Infrared Moon imaging for remote sensing of atmospheric smoke layers

Joseph A. Shaw,[1,*] Paul W. Nugent,[1] and Michael Vollmer[2]

[1]Montana State University, Bozeman, Montana 59717, USA

[2]Brandenburg University of Applied Sciences, Germany

*Corresponding author: jshaw@montana.edu

Simultaneous visible and long-wave infrared (IR) images of the Moon were used with a simple energy-balance model to study the spatial pattern of lunar surface temperatures. The thermal images were obtained with a radiometrically calibrated, compact, low-cost, commercial IR camera mounted on a small telescope. Differences between the predicted and measured maximum Moon temperatures were used to determine the infrared optical depth (OD), which represents the path-integrated extinction of an elevated layer of wildfire smoke in the atmosphere. The OD values retrieved from the IR Moon images were combined with simultaneous OD measurements from a ground-based, zenith-pointing lidar operating at a wavelength of 532 nm to determine an IR-to-visible OD ratio of 0.50 ± 0.18 for moderately aged wildfire smoke aerosol.   © 2014 Optical Society of America

OCIS codes: (010.1100) Aerosol detection; (010.1290) Atmospheric optics; (010.1310) Atmospheric scattering; (010.0280) Remote sensing and sensors; (010.5630) Radiometry.

http://dx.doi.org/10.1364/AO.54.000B64

1. Introduction

The Moon provides some of the most beautiful and easily seen natural optical phenomena at night. For example, scattering by thin clouds passing in front of the Moon can create colorful rings of light surrounding the Moon [1–4]. The Moon itself can provide captivating scenes, especially when it is near the horizon [5,6] or eclipsed by the Earth's shadow [7].

The Moon's prominent role in our visual world naturally leads to interest that can be harnessed for educational purposes. One recent example of this was observations of the Moon with commercial thermal infrared (IR) cameras [8]. That study used basic principles of absorbed and radiated energy balance to predict the maximum lunar surface temperature, and then illustrated that it was possible to obtain reasonable measurements of this temperature using

the simple model and thermal images obtained with increasingly accessible IR cameras. A similar simple model was developed earlier for estimating thermal IR radiance from the Moon in ground-based remote sensing studies [9].

The authors of these two studies recently collaborated to obtain improved IR Moon images for educational purposes. This experiment was designed to achieve several advantages relative to previous measurements [8]: (1) a telescope-mounted thermal camera achieved 100 pixels across the Moon, compared with 15 pixels in the previous study, allowing investigation of how visible patterns of dark and light relate to the spatial distribution of Moon surface temperature; (2) radiosonde and lidar data with MODTRAN calculations provided a more complete atmospheric characterization; and (3) the higher elevation of our experimental site in Bozeman, Montana (1524 m ASL), provided a lower atmospheric attenuation compared with Brandenburg, Germany (<100 m ASL). This paper reports the results of this latest experiment to demonstrate the use of a

low-cost, uncooled, thermal IR camera to obtain high-quality thermal images of the Moon and interpret them with a simple energy-balance model. However, a thin smoke layer high in the atmosphere during our measurements attenuated the observed lunar radiance sufficiently to require compensation before accurate Moon temperature measurements could be obtained. Fortunately, the availability of radiosonde data and lidar measurements provided an opportunity to characterize the atmosphere so that the IR Moon images could be used to retrieve estimates of the smoke-layer optical depth (OD). In the process, we also obtained a valuable estimate of the IR-to-visible OD ratio for moderately aged biomass burning aerosols.

Thermal IR Moon images were acquired on August 1, 2012, at full Moon and on August 3, 2012, two days after the full Moon. The August 3 images were acquired with a cloud-free atmosphere that contained an elevated layer of wildfire smoke from fires burning in Idaho and Montana within a distance of approximately 300 km. These images were used with the model-predicted maximum lunar temperature to retrieve the OD of the smoke layer after removing clear-sky extinction and emission.

The rest of this paper reviews the use of the Moon in remote sensing measurements and instrument calibration, summarizes the simple Moon model used to estimate a maximum Moon surface temperature, describes the measurement and analysis methods used in the study, presents results that include high-quality, radiometrically calibrated IR Moon images and simulated Moon temperature profiles, along with retrievals of the OD for the high-altitude smoke layer, and ends with a discussion of how this approach can be used for educational and research purposes.

2. Moon Used in Remote Sensing

The Moon is increasingly used as a source for calibrating visible and near-infrared (NIR) remote sensing instruments in space [10–16]. In its current situation, the Moon at fixed illumination and observation geometry has been shown to be radiometrically stable within 10^{-8} per year for irradiance and 10^{-7} per year for radiance at common spacecraft imaging instrument resolution in the visible NIR range [12]. Careful visible NIR characterization of the Moon as an absolute radiometric standard as a function of lunar phase angle [11,13] provides common calibration for multiple instruments, even ones that operate at different times [14]. This has led to the routine use of lunar calibrations for instruments such as MODIS, which views the Moon once per month to monitor the long-term stability of its reflective solar bands [15,16].

There also have been efforts to establish thermal IR lunar calibrations. The Moon has relatively smooth spectral variation, emitting as a nearly graybody source for wavelengths beyond about 5 μm [9], with the exception of modest deviations arising from

the Christiansen and SiO_2 features in the nominal range of 7–9.5 μm [10,17]. Lunar calibration is being applied currently to the VIIRS fire-detection band at 4 μm, which has an on-board blackbody calibration source operating at 315 K but requires calibration at higher temperatures because fire detection occurs when the temperature exceeds 343 K [18]. The VIIRS lunar calibration uses an algorithm that includes emission and reflection, with a maximum temperature of 390 K, based on observations from the Lunar Reconnaissance Orbiter Diviner mission—the first instrument to systematically map lunar thermal radiation with diurnal and seasonal variability at wavelengths out to 400 μm [19,20].

The Moon also has been used as a light source for ground-based remote sensing measurements. For example, Earthshine measurements have been used to estimate the Earth disk-averaged shortwave albedo for climate studies [21,22]. Similarly, analysis of *Apollo 15* data suggested that lunar surface temperature measurements on the side facing Earth would contain information about the radiative heat balance of the Earth for climate studies [23]. Also, in the thermal IR spectral range, moon glints have been shown to be an important component of the polarization state of emission measurements from water surfaces [24]. The Moon also has been used as a direct IR light source for ground-based spectroscopic measurements of atmospheric trace gases during the polar night [25,26].

The use of the Moon as an IR source for calibration or remote sensing measurements, however, requires careful consideration of spatial, temporal, and spectral variations in the Moon's emission. For example, deviations from a blackbody spectrum arise because of spatial temperature variations on scales smaller than the observing instrument's field of view [17]. Early optical measurements and laboratory measurements on lunar soil yielded an estimate of 0.89 ± 0.04 for the IR emissivity in the spectral range of 10.5–13.5 μm, but the same paper included a footnote mentioning newer results that estimated the emissivity in the range of 0.93–0.975, and the author estimated that the emissivity uncertainty gave rise to an average surface temperature uncertainty of ± 2 K [10]. Similarly, the annual variation of the Moon–Sun distance induces a temperature variation of approximately ± 1.5 K, which is a systematic variable that can be accounted for easily. Shaw combined some of the results from the literature prior to 1999 to create a simple model of lunar IR emission with a maximum daytime temperature of 390 K and emissivity of approximately 0.98 [9]. More recent observations indicate a maximum daytime temperature of approximately 387 K from the Clementine long-wave IR camera that observed the Moon in a lunar polar orbit [27], 391 K from ground-based measurements [8,28], and up to 395 K from the Diviner mission [19].

In addition to establishing the maximum temperature for a full moon, it is necessary to consider the

variation of temperature with lunar phase and across the lunar disk. Recent observations made with a single-pixel 8–14 μm radiometer mounted at the focal plane of a 20 cm diameter telescope show that the variation with phase can be estimated roughly with a sinusoidal curve [28], but more accurate modeling requires including the opposition effect, which causes the visible Moon to become approximately 40% brighter on the last day before full Moon and the first day after full Moon [29]. This effect is caused by a combination of shadow hiding (particles hiding their own shadows at astronomical opposition) and coherent backscatter (constructive interference of multiply scattered light) [29,30]. Lunar surface roughness on a scale of 1 cm and larger produces a shading effect that alters the illumination and, hence, the thermal spectrum. The general effect in the IR is reduced emission at wavelengths shorter than the emission peak near 8 μm, which alters the apparent brightness temperature [31]. It even has been shown that angular variation of IR emissions can be used to estimate Martian surface roughness on scales from 0.01 to 1 m [32].

While these studies aim to obtain increasingly accurate characterizations of the IR moon, a relatively simple graybody model can be used to obtain a reasonable prediction of temperature profiles across the lunar surface, especially near full moon. This paper shows a favorable comparison of the results of this kind of model with long-wave IR images obtained with a commercial IR camera mounted at the focal plane of a small reflective telescope. To our knowledge, this is the only reported use of a low-cost, commercial IR camera to derive aerosol or smoke OD from images of the Moon.

3. Moon Temperature Model

The lack of atmosphere on the Moon leads to a relatively simple thermal environment in which emission equals absorption. Therefore, lunar thermal emission can be reasonably approximated with a simple calculation based on band-averaged emissivity and solar irradiance. Vollmer and Möllmann [8] recently developed the following expression for predicting the Moon's temperature T_m from the Stefan–Boltzmann law with constant $\sigma = 5.670 \times 10^{-8}$ W/(m^2 K^4), lunar latitude angle φ, band-averaged shortwave albedo α_{vis}, solar irradiance on the Moon E_m, and long-wave emissivity ϵ_{IR}:

$$(1 - \alpha_{\text{vis}})E_m \cos(\varphi) = \epsilon_{\text{IR}} \sigma T_m^4. \qquad (1)$$

Because the Earth–Moon distance is small relative to the Earth–Sun distance, we use the well-established spectrally averaged solar irradiance on Earth (the solar constant) as the solar irradiance on the Moon (i.e., $E_{m\_\text{ave}} = 1361$ W/m^2). We adjust this value to account for the seasonally varying Earth–Sun distance, R_{ES} (whose mean value is $E_{m\_\text{ave}} = 1.496 \times 10^{11}$ m = 1 AU), as follows:

$$E_m(R_{\text{ES}}) = E_{m\_\text{ave}} \left(\frac{1}{R_{\text{ES}}}\right)^2, \qquad (2)$$

with the Earth–Sun distance expressed in AU. The measurements discussed later in this paper were made on August 1 and 3, 2012, at which times the Earth–Sun distances were 1.01477 and 1.01450 AU, respectively, leading to spectrally averaged solar irradiance values of 1321.7 W/m^2 and 1322.4 W/m^2, respectively. At full Moon ± two days, the average shortwave lunar albedo for the Maria regions, where the highest temperatures tend to occur, can be approximated as $\alpha_{\text{vis}} = 0.07$ [19]. Within the uncertainty of this simple model, it is reasonable to assume a value of $\epsilon_{\text{IR}} = 0.93$ for the long-wave emissivity [10,17,33] as an approximate value for the long-wave emissivity. With these assumptions, Eq. (1) leads to an equilibrium temperature for the Moon as a function of latitude angle:

$$T_m(\varphi) = \sqrt[4]{\frac{E_m \cos(\varphi)}{\sigma}} = T_{\max} \cos^{1/4}(\varphi). \qquad (3)$$

Equation (3) is in agreement with results from standard thermal models used for asteroids, which also assume that all surface elements are in instantaneous equilibrium with the incident solar radiation. In addition to our model, thermal asteroid models also introduce the asteroid longitude angle θ [34], finally giving

$$T_m(\varphi, \theta) = T_{\max} \cos^{1/4}(\varphi) \cdot \cos^{1/4}(\theta). \qquad (4)$$

Later on, when analyzing line plots across the lunar disk, we only change one of these angles while keeping the other zero; therefore, Eq. (3) is sufficient for further analysis.

Solving Eqs. (3) or (4) with the irradiance values just mentioned and with $\varphi = \theta = 0$ leads to $T_{\max} = 390.8$ K (117.6°C) for August 1 and 3, 2012, which is in close agreement to the values reported in the literature and discussed earlier in this paper for the maximum lunar temperature.

As explained more fully elsewhere [8], the temperature across the full moon is expected to vary strongly, from the maximum value of approximately 391 K (118°C) at the center, to about 363 K (90°C) at 70% of the lunar radius, and below 323 K (50°C) beyond 90% of the lunar radius for the fully illuminated Moon. The simple model of Eq. (3) can be used to predict the approximate temperature at different locations on the Moon along a line through the center, but it unrealistically predicts a temperature that approaches zero near the edge because it does not include the effects of internal core heating, surface roughness, and so forth. By comparison, the minimum temperature at new Moon is approximately 123 K (−150°C) [28].

Observation angles from Earth are related to the lunar phase angle at the time and date of an

observation and to the lunar latitude angle (see [8]). Therefore, we can quantitatively relate data from line plots within IR images across the lunar disk to the theoretical prediction of Eq. (3) (see Section 4).

4. Measurement and Analysis Methods

A. Moon Imaging

Our measurements are based on thermal IR images acquired using increasingly common uncooled microbolometer-based thermal cameras [35]. The primary Moon-observing camera was a FeathIR Scope system from Polaris Sensor Technologies, Inc. This system incorporates a FLIR Tau 640 long-wave microbolometer camera with 640×512 pixels, mounted inside a small reflective telescope with a 200 mm focal length and f-number of 1.25, producing a $3.1° \times 2.5°$ field of view (FOV). This placed approximately 100 pixels across the lunar disk. Fourteen-bit digital images from the FeathIR Scope system were acquired via USB with a laptop computer. On August 3, we also used a FLIR Photon 640 long-wave microbolometer camera with 640×512 pixels and an $f/1.7$ lens with 50 mm focal length, producing an $18° \times 14°$ FOV that placed approximately 17 pixels across the Moon.

During each image-acquisition cycle in our field experiment, both thermal cameras were sequentially pointed at the Moon, the clear sky, and two large-area blackbody sources operating at 80°C and 15°C at a distance of 20 m from the cameras, as indicated in Fig. 1 (at this distance, the blackbody sources subtended an angle comparable with the Moon's). However, data post-processing revealed that the blackbody source temperatures were not sufficiently stable because of cooling by the outdoor air motion (this problem was removed in subsequent experiments by shielding the blackbody from the wind). Therefore, we relied on a calibration transfer procedure using the well-calibrated Photon 640 as a reference. The Photon 640 camera was carefully calibrated to measure radiance [W/(m² sr)], using methods developed at Montana State University to enable stable operation of uncooled imagers in long-term field deployments [36–38]. These methods were developed originally for high-accuracy radiometric imaging of the atmosphere to determine cloud statistics in climate studies and Earth-space optical communications [39–43]. We used the previously calibrated

Photon 640 camera to determine the actual temperatures for the blackbody images acquired in the field, and then calibrated the FeathIR Scope system using its blackbody images with the adjusted source temperatures. Previous studies suggest that the uncertainty in the camera's output temperature achieved with this approach should be within approximately ±0.25°C [36–38].

Thermal Moon images were acquired on August 1, 3, and 11, 2012, in Bozeman, Montana, USA. As stated previously, the Earth–Sun distance on the two nights near full Moon was approximately 1.015 AU, which corresponds to solar irradiance of 1322 W/m² and angular lunar diameter of 0.526° (the Earth–Sun distance for the crescent Moon on August 11 was 1.013 AU). The Moon was full at 21:28 Mountain Daylight Time (MDT = UTC – 6 h) on August 1. Figure 2 shows the elevation of the Moon center (including atmospheric refraction) as a function of time (MDT) for our measurements on August 1 and 3, 2012.

B. Atmospheric Characterization

An important component of our experiment was determining the atmospheric transmittance and emission to accurately recover the Moon's temperature. In the long-wave IR band of interest for this experiment (~7.5–13.5 μm), the primary effects in a clear atmosphere are attenuation and emission by water vapor, carbon dioxide, and ozone [39]. The most important of these to characterize accurately is water vapor, because of its strong spatial and temporal variability. For this purpose, we launched a radiosonde to measure the vertical profile of temperature and humidity above the Montana State University campus (45.667°N, 111.046°W, 1.524 km above mean sea level). The balloon was launched at 23:24 MDT on the evening of August 3, 2012, and reached its maximum altitude of 21.3 km 1.3 h after launch. Carbon dioxide is a uniformly mixed gas, for which we used a value of 393 ppm, which is an average of the July and August 2012 monthly mean values reported for the Mauna Loa Observatory [44]. The radiosonde profile and CO_2 concentration were used with the US76 Standard Atmosphere model profiles of ozone and other gases in the MODTRAN 5 radiative transfer code [45] to calculate atmospheric transmittance. These calculations produced spectra of atmospheric
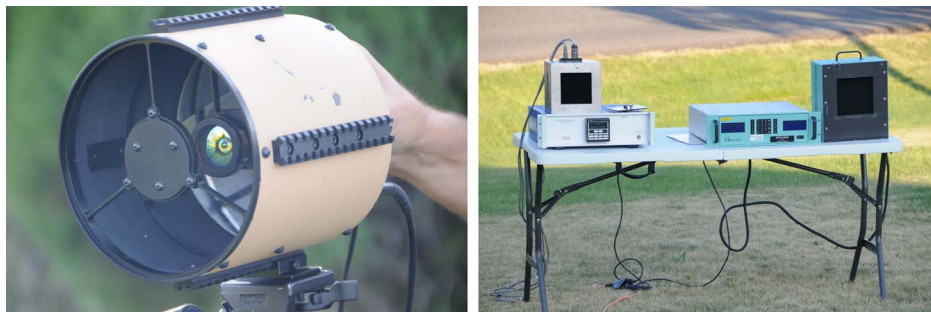

Fig. 1. Infrared camera (left) and blackbody calibration sources (right) used in the August 2012 lunar imaging experiments.
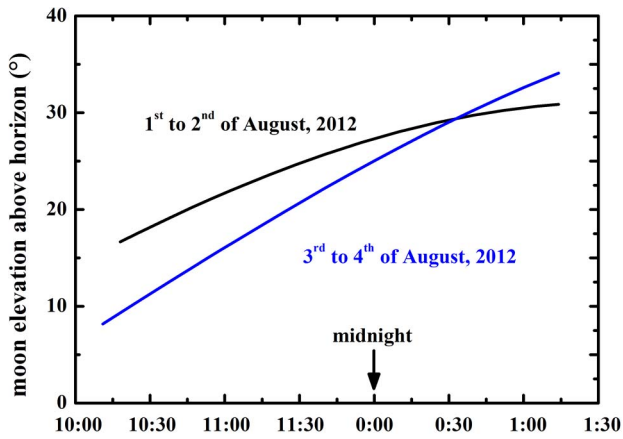
Fig. 2. Lunar elevation as a function of time for observations on August 1 and 3, 2012 (data from Calsky for the observation location).
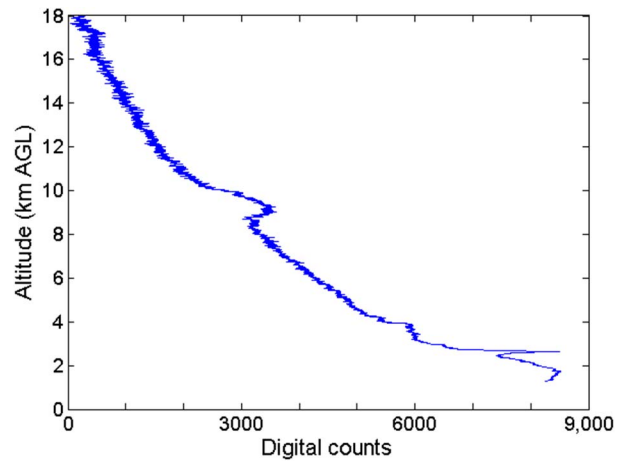

Fig. 4. Vertical profile of relative lidar backscatter signal (1 min average) at 23:00 MDT on August 3, 2012, at Montana State University, showing the presence of a thin smoke layer near 9.5 km AGL and aerosol layers between approximately 2 and 4 km AGL.

transmittance for the slant path from the ground to space in the direction of the Moon for each image (see [39] for further discussion of similar spectra). The spectra shown in Fig. 3 for two different lunar elevation angles illustrate the decreased transmittance and increased clear-sky emission that occur at smaller elevation angles (larger zenith angles). This is because of longer path length or higher air mass, which also gives rise to variations in the visual color of the Moon as it rises or sets [6].

C. Smoke Optical Depth

Because of the high probability of thin smoke layers during late summer at our location, we also operated a zenith-viewing backscatter lidar instrument [46] to detect and measure the smoke OD at a wavelength of 532 nm. Lidar backscatter profiles were processed using an iterative method [47] that was found in previous studies to work well for smoke or clouds with OD less than approximately 2 [48]. Figure 4 is a plot of the relative backscatter signal for the co-polarized lidar channel at 23:00 MDT on August 3, 2012, clearly showing the presence of a primary smoke layer at an altitude of approximately 9.5 km above

mean ground level (AGL), and several thin layers of aerosol (maybe smoke) in the altitude range of 2–4 km AGL (the cross-polarization ratio remained below 0.02, ruling out the possibility that the elevated layer was cirrus [3,46]). Lidar measurements of the 532 nm smoke OD are presented in the next section.

The radiance L observed by a ground-based thermal camera viewing the Moon through the atmosphere with a thin smoke layer is a combination of the radiance L_{moon} emitted by the Moon and transmitted through the atmosphere, the radiance L_{atm} emitted by the clean atmosphere along the slant path to the Moon, and the radiance L_{smoke} emitted by the smoke along the same slant path. The Moon radiance, L_{moon}, includes attenuation by the clean atmosphere (discussed below), but is multiplied by an exponential term accounting for the further attenuation arising from passage through a smoke layer with zenith-path OD τ_{smoke} and a slant-path air mass M (estimated from the zenith angle θ_z using a
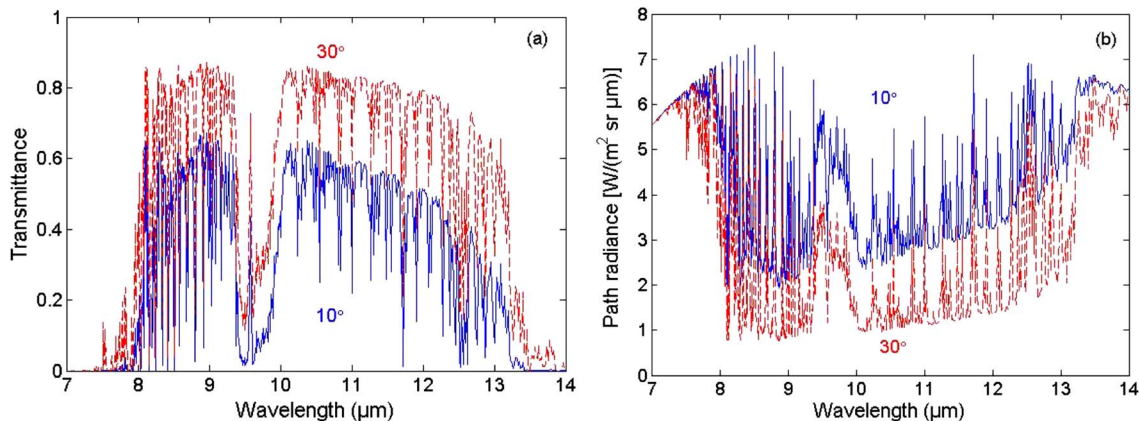

Fig. 3. MODTRAN calculations of (a) atmospheric transmittance and (b) atmospheric emitted radiance along an Earth-space path from Bozeman in the direction of the Moon at elevation angles of 10° and 30°, using radiosonde input for the night of August 3, 2012.

refraction-based model [6,49]):

$$L = L_{moon}e^{-\tau_{smoke}M} + (L_{atm} + L_{smoke}). \quad (5)$$

Experimentally, we obtained the atmospheric and smoke radiance $L_{atm} + L_{smoke}$ from a clear-sky pixel adjacent to and at the same zenith angle as the Moon. We then solved Eq. (5) to obtain the smoke OD, τ_{smoke}:

$$\tau_{smoke} = -\frac{1}{M}\ln\left[\frac{L - (L_{atm} + L_{smoke})}{L_{moon}}\right]. \quad (6)$$

Each radiance term is a band-averaged quantity that depends on the sensor's spectral response function $f(\lambda)$, and the smoke-layer OD is not expected to have fine spectral structure, so the exponential model is reasonable in Eqs. (5) and (6). However, as Fig. 3 shows, the atmospheric transmittance has fine spectral structure that was modeled using local radiosonde data in the MODTRAN5 code, as described in Section 4B, and integrated over the camera spectral response function, as indicated in the following two equations.

The atmospheric-attenuated Moon radiance L_{moon} can be described in terms of the sensor spectral response function $f(\lambda)$, Moon emissivity $\epsilon_m(\lambda)$, blackbody spectral radiance L^{bb} for the Moon temperature T_m, and atmospheric transmittance t_{atm} at the Moon's zenith angle θ_z:

$$L_{moon} = \int f(\lambda)\epsilon_m(\lambda)L^{bb}(\lambda, T_m)t_{atm}(\lambda, \theta_z)d\lambda. \quad (7)$$

The observed clear-sky radiance L_{atm} was obtained as part of the signal from a clear-sky pixel, but can be described in terms of the sensor spectral response function $f(\lambda)$ and the clean-atmosphere radiance L_a at zenith angle θ_z:

$$L_{atm} = \int f(\lambda)L_a(\lambda, \theta_z)d\lambda. \quad (8)$$

The observed smoke-layer radiance L_{smoke} also was part of the clear-sky pixel measurement, but can be described in terms of the sensor spectral response function $f(\lambda)$, the radiance L_s emitted by the smoke layer, and the transmittance t_{atm2} for the atmospheric path between the smoke layer and the ground:

$$L_{smoke} = \int f(\lambda)L_s(\lambda, \theta_z)t_{atm2}(\lambda, \theta_z)d\lambda. \quad (9)$$

In summary, finding the smoke-layer OD with Eq. (6) required the following steps:

1. Calibrate raw thermal images to IR radiance L (as discussed previously, the well-calibrated Photon 640 was used as a transfer standard to adjust the blackbody images used to calibrate the FeathIR Scope system).

2. Subtract from L the radiance for a clear-sky pixel adjacent to the Moon ($L_{atm} + L_{smoke}$).

3. Calculate IR atmospheric spectral transmittance t_{atm} with MODTRAN5 using radiosonde data (the sum of clean-atmosphere and smoke emission were measured together at a clear-sky pixel when deriving the smoke OD in step 2, but the radiance emitted by the atmosphere also was calculated with MODTRAN5 to enable the image processing shown in Figs. 8–10 before consideration of the smoke layer).

4. Divide the difference $L - (L_{atm} + L_{smoke})$ by the band-average Moon radiance L_{moon}, calculated from Eq. (7) using the atmospheric transmittance t_{atm}.

5. To obtain the IR smoke OD, τ_{smoke}, divide the logarithm of the quotient by the air mass M calculated from a refraction model using the zenith angle at the center of the Moon [6,49].

5. Results

A. Analysis Neglecting Smoke

Images of the full Moon acquired from visible and thermal cameras on the nights of August 1 and 2, 2012, are shown in Fig. 5, with the Moon more than 99.9% illuminated. The visible image was obtained at 00:52 MDT on August 2, 2012, using a Nikon D300 camera with a Nikon 80–400 mm zoom lens set at 400 mm focal length, which produced a 3.4° horizontal FOV (camera settings were $f/11$, ISO 1250, 1/500 s). The thermal IR image was obtained at 01:05 MDT on August 4, 2012, using a laptop computer with the FeathIR Scope system with 3.1° horizontal FOV. Both images have been cropped to highlight the Moon. The thermal image has been processed to remove atmospheric extinction and emission, but it is not corrected for smoke aerosol effects. It is displayed with colors that represent temperature in K, found as the temperature of a graybody source that emits the same band-integrated radiance as measured from each pixel of the thermal image.
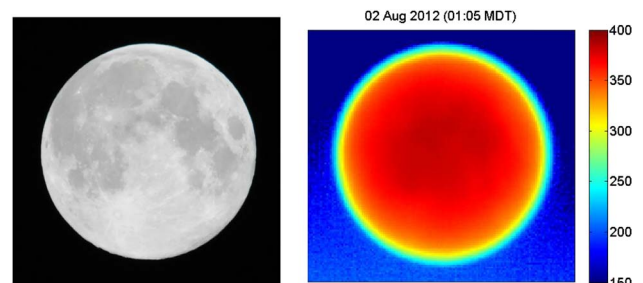

Fig. 5. Images of full Moon at 30° elevation angle. (a) Visible photograph from Nikon D300 camera with Nikon 80–400 mm lens set at 400 mm, 3.4 h after full Moon at 00:52 MDT (06:52 UTC) on August 2, 2012. (b) IR image processed according to details in text but displayed in units of temperature in K from FeathIR Scope system with 3.1° horizontal field of view at 01:05 MDT on August 2, 2012 (images cropped to emphasize Moon).
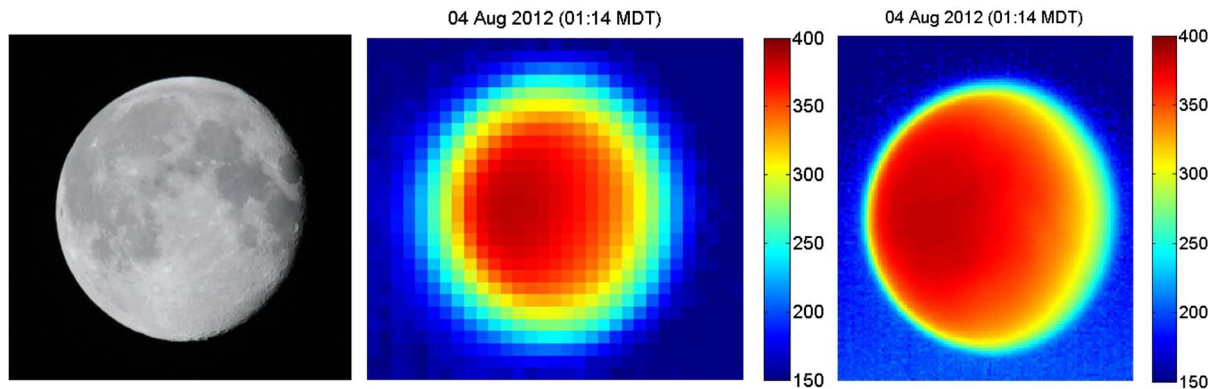
Fig. 6. Images for two nights after full Moon (34° elevation angle). (a) Visible photograph from Nikon D300 camera with Nikon 80–400 mm lens at 400 mm, 51.8 h after full Moon, 01:15 MDT (07:15 UTC) on August 4, 2012. (b) Processed IR temperature image from FLIR Photon 640 camera with 18° horizontal field of view, 01:14 MDT on August 4, 2012. (c) Processed IR temperature image from FeathIR Scope system with 3.1° horizontal field of view, 01:14 MDT on August 4, 2012 (all images cropped to emphasize Moon).

Figure 6 shows images acquired on the nights of August 3 and 4, 2012, two nights after full Moon (approximately 94.6% illuminated). The left-hand panel is a visible image taken at 01:15 MDT on August 4, 2012, with a Nikon D300 camera and 80–400 mm lens set at 400 mm (f/11, ISO 1250, 1/640 s). The center panel is a thermal IR image acquired at 01:14 MDT on August 4, 2012, with the Photon 640 camera, which provided an 18° horizontal FOV. The right-hand panel is a thermal IR image acquired at the same time with the FeathIR system, with the atmospheric extinction and emission effects removed (but with no smoke correction). There is a clearly apparent spatial resolution advantage of the FeathIR system, but the Photon 640 image still accurately identifies the centroid location for the region of maximum temperature.

One final example is shown in Fig. 7, which is a thermal image of the crescent Moon, for which the lunar surface was 32.1% illuminated. This image was acquired with the FeathIR Scope system at 16:59 MDT on August 11, 2012 (near midday),

231.5 h after full Moon. An approximate correction for atmospheric extinction and emission has been applied to yield a maximum Moon temperature of 291.3 K (the uncertainty is higher for the temperatures on August 1 and 11 because of the lack of radiosonde data on those nights). Note that the maximum observable temperature in this case is less than the absolute maximum Moon temperature, which occurs at a location that is not visible with this viewing geometry.

Horizontal profiles of thermal images from the nights of August 1 and 3, 2012, are plotted with theoretical predictions from Eq. (3) in Figs. 8 and 9 (these profiles, which do not yet account for smoke aerosols, are from processed thermal IR images near the same time as those shown in Figs. 5 and 6). The profile shapes from the high-resolution images acquired with the FeathIR Scope system agree quite well with the simple theory of Eq. (3), but the lower-resolution images acquired with the Photon 640 camera only agree well with the theory near the region of maximum temperature. The theoretical curve in Fig. 8 is symmetric about the center of the Moon, but the corresponding thermal image exhibits a small
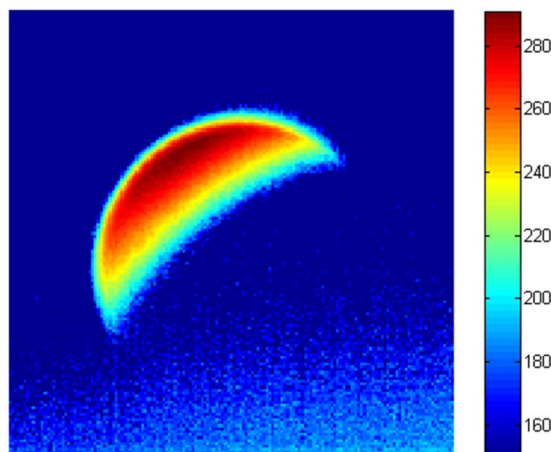

Fig. 7. Processed IR temperature image of the crescent Moon at 32° elevation angle, 12:59 MDT on August 11, 2012 (231.5 h after full Moon), corrected for atmospheric transmittance by scaling the August 3 radiosonde to match surface meteorological readings.
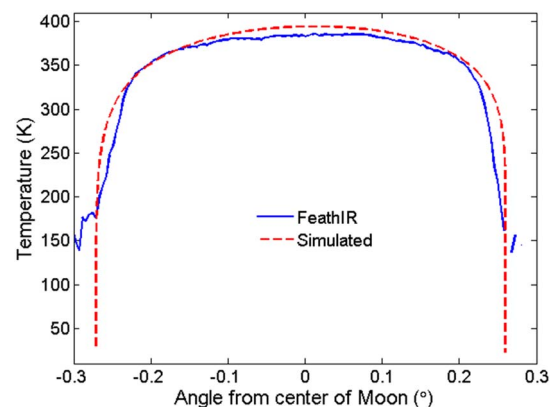

Fig. 8. Horizontal profile across center of thermal Moon image at 23:07 MDT on August 1, 2012 (1.7 h after full Moon), near the time of Fig. 5, showing FeathIR Scope data (solid blue line) and simulation (dashed red line).
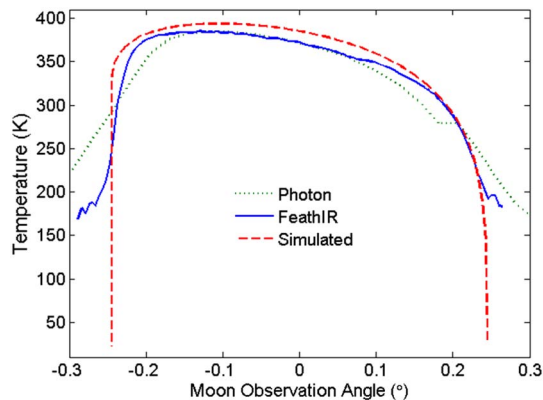
Fig. 9. Horizontal profile across center of thermal Moon images at 01:14 MDT on August 4, 2012 (near the time of Fig. 6), showing FeathIR Scope data (solid blue line), Photon 640 data (dotted green line), and the simulation (dashed red line).
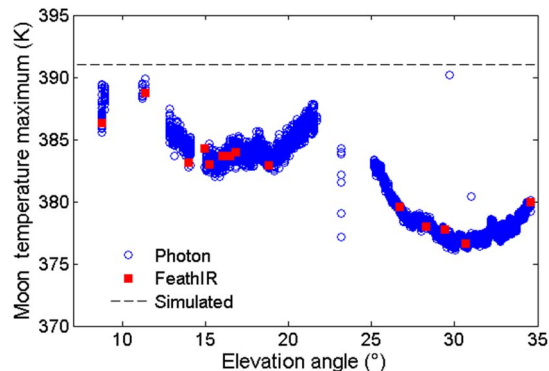

Fig. 10. Maximum Moon temperature obtained from thermal images after compensation for clear-sky atmospheric extinction and emission. The gap between angles of 22°–25° was caused by a cloud moving across the Moon.

asymmetry, with slightly higher temperatures on the left side in the vicinity of −0.2° because of the higher fraction of darker maria on that side of the Moon. Beyond the Moon edges at approximately ±0.25°, the temperature from the high-resolution thermal images flares outward for multiple pixels, as was discussed previously [8]. Figure 9 shows the region of maximum temperature shifted notably to the left of center, toward the sun-illuminated region. We also tried adding temperature profiles calculated from DIVINER data, but we found that there were significant differences that apparently arose as a result of the non-Lambertian lunar surface being viewed at different angles by our Earth-based cameras and the Moon-orbiting satellite-based sensor.

B. Estimating Smoke Optical Depth

The maximum temperatures from the IR image profiles in Figs. 8 and 9 were always below the theoretical values by a variable amount up to 15 K. This is a result of attenuation of the Moon radiance as it passed through smoke aerosol layers in the atmosphere, which were not yet included in the analysis. The maximum Moon temperatures derived from thermal images before correction for the smoke extinction (but after correction for calculated nonsmoke atmospheric attenuation and emission) are plotted versus Moon elevation angle in Fig. 10 for the night of August 3 and 4, 2012. The blue circle symbols are measurements from the Photon 640 camera, and the red squares are measurements from the FeathIR Scope system; the horizontal dashed line marks the theoretical maximum Moon temperature of 390.8 K found in Section 2 using Eq. (3). At the start of the measurement sequence, the Moon temperatures from the thermal images were relatively close to the theoretical value, but they became notably lower for elevation angles above 12°, reaching a minimum of 376 K at about 30° elevation angle. The closest agreement occurred just below 12° elevation angle, when the thermal-image-derived Moon temperature reached approximately 390 K. The variability

demonstrates that the difference from the theoretical Moon temperature is not a systematic error, but is instead consistent with temporally variable smoke extinction. Between 23:45 and 00:00 (22° and 25°), data are missing, since a cloud was passing through the camera FOV (the data points included in this gap period indicate the high variability of the aerosols when clouds were nearby).

Occasionally, on the nights of August 3 and 4, the smoke layer could be slightly discerned in visible photographs of the Moon, but it was mostly not visually apparent, either by eye or on photographs. The optically thin nature of the smoke also was indicated by daytime solar radiometer measurements of visible aerosol OD values (at 500 nm wavelength) of approximately 0.054 at sunset on August 3, 2012 (the peak aerosol OD on that day was 0.11 at sunrise). On the nights of August 3 and 4, 2012, the 532 nm lidar measurements of aerosol OD were in the range of 0.05 to 0.10, also similar to the solar radiometer measurements of aerosol OD on the following day, which varied between 0.032 and 0.085.

To estimate the IR smoke OD for a 10 μm mean wavelength, τ_{smoke} was adjusted to make the right-hand side of Eq. (5) match the radiance measured in the appropriate pixels of the IR Moon image (using the theoretically derived maximum Moon temperature of 390.8 K to determine L_{moon}). The IR smoke OD values derived in this manner from thermal Moon images are plotted in Fig. 11 as a function of time (MDT), together with lidar measurements that were filtered with a 10 min sliding median filter and then converted to IR equivalent smoke OD values (black triangles). The IR equivalent smoke OD was obtained by multiplying the 532 nm values by an IR-to-visible ratio of 0.50 ± 0.18, found as the mean of the ratios of 10 min averages of IR Moon image OD and median-filtered 532 nm lidar OD. The 0.18 uncertainty in this mean value is the result of a standard error propagation calculation based on the standard deviations of the numerator and denominator of the ratio.
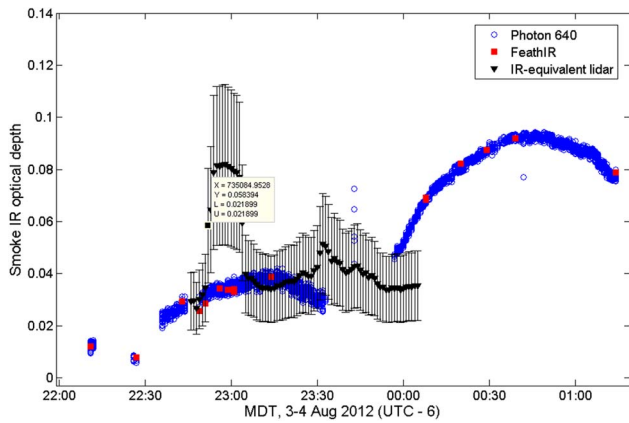
Fig. 11. IR smoke optical depth (10 μm wavelength) estimated from thermal Moon images and lidar on the nights of August 3 and 4, 2012.

The IR equivalent smoke OD from the lidar, shown in Fig. 11, had a mean of 0.044, median of 0.038, and standard deviation of 0.015. The IR smoke OD derived from the thermal Moon images (also Fig. 11) had a mean of 0.037, median of 0.035, and standard deviation of 0.0073. Dividing the mean of the image-derived IR smoke OD by the IR-to-visible ratio (0.50) produces a mean visible-equivalent smoke OD of 0.074 during our nighttime measurement sequence. This compares well with daytime solar radiometer measurements of aerosol OD of approximately 0.06 near sunset on August 3 and between approximately 0.032 and 0.085 during the day of August 4. Particularly good agreement is found by comparing the image-derived, visible-equivalent smoke OD value at about 10.40 MDT (0.022/0.50 = 0.044) with the pre-sunset solar radiometer OD reading of 0.054 from 3 h earlier (keep in mind also that, even with the same instrument, the smoke OD is expected to be slightly larger at the 500 nm solar radiometer wavelength than at the 532 nm lidar wavelength).

Table 1 lists values for the radiances, temperatures, and atmospheric transmittances for thermal Moon images at elevation angles of 9°, 20°, and 30°, covering the range of observations from the nights of August 3 and 4, 2012. The columns are labeled with variables from Eqs. (5) to (7), with the new variables T_m^* representing the apparent maximum Moon temperature with no smoke compensation (shown in Fig. 10) and L_{exo} representing the exo-atmospheric radiance of the measured signal after subtracting atmosphere and smoke emission and dividing by the atmospheric transmittance (but without correcting for the smoke extinction). In the absence of

smoke, this value would be expected to be approximately 124 W/(m² sr), which is the camera-specific band-average radiance corresponding to the theoretical maximum Moon temperature of 390.8 K. The last two columns represent the sensitivity of retrieved smoke OD on radiance uncertainties, as discussed below.

When interpreting the trends of the data in Table 1, it is important to remember that the smoke was changing during this time period, so the values in the table do not change solely with increasing elevation angle. This is shown, for example, by the changing apparent Moon temperatures in Fig. 10 (T_m^*), indicating that the smoke OD started out very low, increased at lunar elevation angles above 12°, decreased briefly for angles above about 20°, and increased again for angles above about 22°. Examination of the numbers in the table also reveals the importance of careful atmospheric characterization.

To estimate the sensitivity of the retrieved IR smoke OD on radiance changes, we calculated the OD change that would result from a change in the exo-atmospheric Moon radiance, L_{exo}. The results are shown in the last two columns of Table 1. The column labeled $\Delta\tau_{0.25}$ shows the change in OD resulting from a 0.25 W/(m² sr) radiance change, which corresponds to the IR camera calibration uncertainty [36–38]. This gives rise to an OD uncertainty that varies from 0.8% for the highest OD values observed here to 2.4% for the lowest OD values. The column labeled $\Delta\tau_{1.0}$ shows that the OD uncertainty for a 1.0 W/(m² sr) radiance change, corresponding to the total approximate uncertainty in the calibration and atmospheric characterization, varies from 5.4% to 9.6% for our observed values. It is important to note also that this method depends significantly on the accuracy of the lunar long-wave emissivity, short-wave albedo, and resulting theoretical maximum temperature. For example, changing $\varepsilon_{\mathrm{IR}}$ or α_{vis} by ±0.01 causes the maximum Moon temperature $T_{\max}$ to change by ±1.1 K. Similarly, changing $\varepsilon_{\mathrm{IR}}$ or α_{vis} by ±0.03 causes the temperature to change by approximately ±3.2 K).

6. Discussion

The procedure described here to extract the IR smoke OD from IR Moon images shows promise for remote sensing of smoke or other aerosols in the atmosphere. The simple Moon model serves as an easily understood educational tool and may be sufficient for some remote sensing applications, but also contributes some of the largest uncertainties in the results presented here. Future implementations could

Table 1. Component Values in Eq. (6) for Three Measurements on August 3 and 4, 2012[a]

Elevation (°)	L	L_{atm}	L_{smoke}	L_{exo}	T_m^* (K)	τ_{smoke}	$\Delta\tau_{0.25}$ (%)	$\Delta\tau_{1.0}$ (%)
9	54.0	24.0	0.6	113.1	380.9	0.014	2.4	9.6
20	67.4	17.3	0.91	111.8	379.7	0.035	2.1	8.5
30	69.8	14.6	1.17	103.9	372.3	0.088	0.79	5.4

[a][radiance in W/(m² sr)].

benefit from the use of a more sophisticated Moon model, perhaps incorporating librations and spatially variable albedo and emissivity. The other most significant uncertainty arises because the zenith-pointing lidar samples a different portion of the smoke layer than is seen at the same time by the Moon-viewing IR camera. An obvious solution would be to use a scanning lidar system pointed nominally toward the Moon, but this was not possible in our experiment because of limitations imposed by air-traffic control regulations. Instead, we relied on averaging data for 10 min, long enough for the smoke sampled at the zenith to move into the vicinity of the Moon.

The IR-to-visible OD ratio found here (0.50 ± 0.18) is a new contribution for moderately aged biomass smoke aerosol. It is similar to ratios found by others; for example, a ratio of 0.38 ± 0.17 can be inferred from Fig. 4(b) of measurements reported for marine aerosols in East Asia [50], a ratio of 0.35 was found to decrease to 0.22 during transport for elevated Saharan dust layers using AIRS satellite data [51], and ratios of 0.34, 0.37, and 0.59 were found for Saharan dust using three different dust models with airborne measurements [52]. Also, an IR-to-visible OD ratio on the order of 0.5 ± 0.05 is frequently used for cirrus clouds [53] (a result we use to estimate visible cloud OD from thermal cloud images [48]).

Comparison of visible and IR images of the moon show two important features. First, from the images in Fig. 5, it can be seen that the maximum temperature of the full Moon appears slightly above the centerline, in the region where the darker maria regions are seen in the visible image. The darker appearance of these regions indicates a lower short-wave albedo, which leads to increased absorption and thermal emission. Second, the images in Figs. 6 and 7 show that the location of the maximum temperature for the partially illuminated Moon is driven primarily by the illumination angle and secondarily by the spatial pattern of visible albedo. This supports the assumptions made in our simple model.

In future work, the OD analysis could be improved. A possible method of reducing the differences in instantaneous images and lidar measurements would be to move the IR camera away from the lidar location, in a direction opposite the Moon, so that the slant path viewed by the IR camera would overlap the region where the smoke layer was sampled by the zenith-pointing lidar. This would require moving the camera throughout the night, but could provide data to estimate an IR-to-visible OD ratio with lower uncertainty. Then, in future implementations, the IR camera could be used alone in a fixed location.

Finally, if a relationship were established between the smoke OD and emissivity, it might be possible to estimate the altitude of the layer by determining the atmospheric temperature that would produce a match between the radiance emitted by the smoke to the product of the retrieved band-average emissivity and the blackbody radiance at the air temperature.

This could, for example, rely on a lapse-rate estimate or a radiosonde measurement of the vertical air temperature profile.

7. Conclusion

Radiometrically calibrated thermal IR images have been used to reveal spatial and temporal variations of surface temperatures on the Moon and, together with a simple model, were used for remote sensing of a smoke aerosol layer in the atmosphere. By combining IR smoke OD values from the IR camera with visible-wavelength smoke OD values from a lidar, a new estimate of 0.50 ± 0.18 was found for the IR-to-visible OD ratio of moderately aged biomass burning aerosol. The smoke OD values retrieved from thermal Moon images were shown to have a maximum uncertainty less than 10%. This Moon imaging method requires sufficient spatial resolution such that the pixels used to determine lunar temperature are observing a value sufficiently close to the maximum temperature. Away from the center of the lunar disk, there are progressively lower temperatures, so larger pixels will give a spatially averaged value that is more difficult to interpret. Observations taken within several days on either side of the full Moon have notable asymmetries in their temperature profile, but are still easily used for this kind of remote sensing if the analysis is restricted to the region of maximum temperature. Without a more accurate model to predict the maximum temperature of a crescent Moon, performing this kind of remote sensing with images with less than a half Moon, such as Fig. 7, would be difficult. With our approach, a good guideline is to have at least three-quarters of the Moon illuminated, as seen from the Earth, but this depends on the spatial resolution provided by the thermal camera and lens. For good quantitative analysis of the maximum temperature pixel, at least two pixels on each side should also detect the same temperature, meaning that a total of five adjacent pixels are required to have essentially the same temperature.

References

1. J. A. Shaw and P. J. Neiman, "Coronas and iridescence in mountain wave clouds," Appl. Opt. **42**, 476–485 (2003).
2. L. Cowley, P. Laven, and M. Vollmer, "Rings around the sun and moon: coronae and diffraction," Phys. Educ. **40**, 51–59 (2005).
3. J. A. Shaw and N. J. Pust, "Icy wave-cloud lunar corona and cirrus iridescence," Appl. Opt. **50**, F6–F11 (2011).
4. P. Laven, "Re-visiting the atmospheric corona," Appl. Opt. **53**, B46–B53 (2014).
5. L. Kaufman and I. Rock, "The moon illusion I," Science **136**, 953–961 (1962).

6. M. Vollmer and S. Gedzelman, "Colors of the sun and moon: the role of the optical air mass," Eur. J. Phys. **27**, 299–309 (2006).

7. N. Hernitschek, E. Schmidt, and M. Vollmer, "Lunar eclipse photometry: absolute luminance measurements and modeling," Appl. Opt. **47**, H62–H71 (2008).

8. M. Vollmer and K. P. Möllmann, "Surface temperatures of the Moon: measurements with commercial infrared cameras," Eur. J. Phys. **33**, 1703–1719 (2012).

9. J. A. Shaw, "Modeling infrared lunar radiance," Opt. Eng. **38**, 1763–1764 (1999).

10. J. L. Linsky, "The Moon as a proposed radiometric standard for microwave and infrared observations of extended sources," Astrophys. J. Suppl. Ser. **216**, 163–204 (1973).

11. H. H. Kieffer and R. L. Wildey, "Establishing the Moon as a spectral radiance standard," J. Atmos. Ocean. Technol. **13**, 360–375 (1996).

12. H. H. Kieffer, "Photometric stability of the lunar surface," Icarus **130**, 323–327 (1997).

13. H. H. Kieffer and T. C. Stone, "The spectral irradiance of the Moon," Astron. J. **129**, 2887–2901 (2005).

14. H. H. Kieffer, T. C. Stone, R. A. Barnes, S. Bender, R. E. Eplee, J. Mendenhall, and L. Ong, "On-orbit radiometric calibration over time and between spacecraft using the Moon," Proc. SPIE **4881**, 287–298 (2003).

15. J. Sun, X. Xiong, B. Guenther, and W. Barnes, "Radiometric stability monitoring of the MODIS reflective solar bands using the Moon," Metrologia **40**, S85–S88 (2003).

16. J.-Q. Sun, X. Xiong, W. L. Barnes, and B. Guenther, "MODIS reflective solar bands on-orbit lunar calibration," IEEE Trans. Geosci. Remote Sens. **45**, 2383–2393 (2007).

17. K. J. Vogler, P. E. Johnson, and R. W. Shorthill, "Modeling the non-grey-body thermal emission from the full Moon," Icarus **92**, 80–93 (1991).

18. J. McIntire, B. Efremova, and X. Xiong, "Calibration of NPP VIIRS fire detection band using lunar observations," Proc. SPIE **8533**, 85331B (2012).

19. A. R. Vasavada, J. L. Bandfield, B. T. Greenhagen, P. O. Hayne, M. A. Siegler, J.-P. Williams, and D. A. Paige, "Lunar equatorial surface temperatures and regolith properties from the Diviner Lunar Radiometer Experiment," J. Geophys. Res. **117**, E00H18 (2012).

20. D. A. Paige, M. C. Foote, B. T. Greenhagen, J. T. Schofield, S. Calcutt, A. R. Vasavada, D. J. Preston, F. W. Taylor, C. C. Allen, K. J. Snook, B. M. Jakosky, B. C. Murray, L. A. Soderblom, B. Jau, S. Loring, J. Bulharowski, N. E. Bowles, I. R. Thomas, M. T. Sullivan, C. Avis, E. M. De Jong, W. Hartford, and D. J. McCleese, "The Lunar Reconnaissance Orbiter Diviner lunar radiometer experiment," Space Sci. Rev. **150**, 125–160 (2010).

21. J. Qiu, P. R. Goode, E. Pallé, V. Yurchyshyn, J. Hickey, P. Montañés Rodriguez, M.-C. Chu, E. Kolbe, C. T. Brown, and S. E. Koonin, "Earthshine and the Earth's albedo: 1. Earthshine observations and measurements of the lunar phase function for accurate measurements of the Earth's Bond albedo," J. Geophys. Res. **108**, 4709–4730 (2003).

22. E. Pallé, P. Montañés Rodriguez, P. R. Goode, J. Qiu, V. Yurchyshyn, J. Hickey, M.-C. Chu, E. Kolbe, C. T. Brown, and S. E. Koonin, "The Earthshine Project: update on photometric and spectroscopic measurements," Adv. Space Res. **34**, 288–292 (2004).

23. S. Huang, "Surface temperatures at the nearside of the Moon as a record of the radiation budget of Earth's climate system," Adv. Space Res. **41**, 1853–1860 (2008).

24. J. A. Shaw, "Degree of linear polarization in spectral radiances from water-viewing infrared radiometers," Appl. Opt. **38**, 3157–3165 (1999).

25. J. Notholt, R. Neuber, O. Schrems, and T. V. Clarmann, "stratospheric trace gas concentrations in the Arctic polar night derived by FTIR-spectroscopy with the Moon as IR light source," Geophys. Res. Lett. **20**, 2059–2062 (1993).

26. J. Notholt, "The Moon as a light source for FTIR measurements of stratospheric trace gases during the polar night: application for HNO_3 in the Arctic," J. Geophys. Res. **99**, 3607–3614 (1994).

27. S. L. Lawson, B. M. Jakosky, H.-S. Park, and M. T. Mellon, "Brightness temperatures of the lunar surface: calibration and global analysis of the Clementine long-wave infrared camera data," J. Geophys. Res. **105**, 4273–4290 (2000).

28. A. H. Maghrabi, "On the measurements of the moon's infrared temperature and its relation to the phase angle," Adv. Space Res. **53**, 339–347 (2014).

29. B. Hapke, R. Nelson, and W. Smythe, "The opposition effect of the Moon: coherent backscatter and shadow hiding," Icarus **133**, 89–97 (1998).

30. D. F. Winter and J. A. Krupp, "Directional characteristics of infrared emission from the Moon," The Moon **2**, 279–292 (1971).

31. P. E. Johnson, K. J. Vogler, and J. P. Gardner, "The effect of surface roughness on lunar thermal emission spectra," J. Geophys. Res. **98**, 20825–20829 (1993).

32. J. L. Bandfield and C. S. Edwards, "Derivation of Martian surface slope characteristics from directional thermal infrared radiometry," Icarus **193**, 139–157 (2008).

33. F. H. Murcray, D. G. Murcray, and W. J. Williams, "Infrared emissivity of lunar surface features 1. Balloon-borne observations," J. Geophys. Res. **75**, 2662–2669 (1970).

34. L. A. Lebofsky, M. V. Sykes, E. F. Tedesco, G. J. Veeder, D. L. Matson, R. H. Brown, J. C. Gradie, M. A. Feierberg, and R. J. Rudy, "A refined "standard" thermal model for asteroids based on observations of 1 Ceres and 2 Pallas," Icarus **68**, 239–251 (1986).

35. M. Vollmer and K.-P. Möllmann, *Infrared Thermal Imaging: Fundamentals, Research and Applications* (Wiley, 2010).

36. P. W. Nugent and J. A. Shaw, "Calibration of uncooled LWIR microbolometer imagers to enable long-term field deployment," Proc. SPIE **9071**, 90710V (2014).

37. P. W. Nugent, J. A. Shaw, and N. J. Pust, "Correcting for focal-plane-array temperature dependence in microbolometer infrared cameras lacking thermal stabilization," Opt. Eng. **52**, 061304 (2013).

38. P. W. Nugent, J. A. Shaw, and N. J. Pust, "Radiometric calibration of infrared imagers using an internal shutter as an equivalent external blackbody," Opt. Eng., to be published.

39. J. A. Shaw and P. W. Nugent, "Physics principles in radiometric infrared imaging of clouds in the atmosphere," Eur. J. Phys. **34**, S111–S121 (2013).

40. P. W. Nugent, J. A. Shaw, and S. Piazzolla, "Infrared cloud imager development for atmospheric optical communication characterization, and measurements at the JPL Table Mountain Facility," IPN Progress Report 42-192, 2013, available at http://tmo.jpl.nasa.gov/progress_report/42-192/192C.pdf.

41. P. W. Nugent, J. A. Shaw, and S. Piazzolla, "Infrared cloud imaging in support of Earth-space optical communication," Opt. Express **17**, 7862–7872 (2009).

42. J. A. Shaw, P. W. Nugent, N. J. Pust, B. Thurairajah, and K. Mizutani, "Radiometric cloud imaging with an uncooled microbolometer thermal infrared camera," Opt. Express **13**, 5807–5817 (2005).

43. B. Thurairajah and J. A. Shaw, "Cloud statistics measured with the Infrared Cloud Imager (ICI)," IEEE Trans. Geosci. Remote Sens. **43**, 2000–2007 (2005).

44. P. Tans and R. Keeling, "Trends in atmospheric carbon dioxide," 2014, http://www.esrl.noaa.gov/gmd/ccgg/trends/#mlo_full.

45. A. Berk, G. P. Anderson, P. K. Acharya, L. S. Bernstein, L. Muratov, J. Lee, M. Fox, S. M. Adler-Golden, J. H. Chetwynd, M. L. Hoke, R. B. Lockwood, J. A. Gardner, T. W. Cooley, C. C. Borel, and P. E. Lewis, "MODTRAN 5: a reformulated atmospheric band model with auxiliary species and practical multiple scattering options: update," Proc. SPIE **5806**, 662–667 (2005).

46. N. L. Seldomridge, J. A. Shaw, and K. S. Repasky, "Dual-polarization lidar using a liquid crystal variable retarder," Opt. Eng. **45**, 106202 (2006).

47. S. A. Young, "Analysis of lidar backscatter profiles in optically thin clouds," Appl. Opt. **34**, 7019–7031 (1995).

48. J. A. Shaw, P. W. Nugent, N. J. Pust, B. J. Redman, and S. Piazzolla, "Cloud optical depth measured with ground-based uncooled infrared imagers," Proc. SPIE **8523**, 85231D (2012).

49. A. T. Young, "Air mass and refraction," Appl. Opt. **33**, 1108–1109 (1994).
50. K. M. Markowicz, P. J. Flatau, A. M. Vogelmann, P. K. Quinn, and E. J. Welton, "Clear-sky infrared aerosol radiative forcing at the surface and the top of the atmosphere," Q. J. R. Meteorol. Soc. **129**, 2927–2947 (2003).
51. C. Pierangelo, A. Chédin, S. Heilliette, N. Jacquinet-Husson, and R. Armante, "Dust altitude and infrared optical depth from AIRS," Atmos. Chem. Phys. **4**, 1813–1822 (2004).
52. E. Highwood, J. M. Haywood, M. D. Silverstone, S. M. Newman, and J. P. Taylor, "Radiative properties and direct effect of Saharan dust measured by the C-130 aircraft during Saharan Dust Experiment (SHADE), 2. Terrestrial spectrum," J. Geophys. Res. **108**, 8578–8590 (2003).
53. D. H. DeSlover, W. L. Smith, P. K. Piironen, and E. W. Eloranta, "A methodology for measuring cirrus cloud visible-to-infrared spectral optical depth ratios," J. Atmos. Ocean. Technol. **16**, 251–262 (1999).